Journal of Magnetic Resonance **148,** 442–448 (2001)
doi:10.1006/jmre.2000.2267, available online at http://www.idealibrary.com on IDEAL®

High-Precision Mapping of the Magnetic Field Utilizing the Harmonic Function Mean Value Property

Lin Li and John S. Leigh

Department of Biochemistry and Molecular Biophysics, and Metabolic Magnetic Resonance Research & Computing Center, Department of Radiology, University of Pennsylvania, Philadelphia, Pennsylvania 19104

Received June 15, 2000; revised November 20, 2000

The spatial distributions of the static magnetic field components and MR phase maps in space with homogeneous magnetic susceptibility are shown to be harmonic functions satisfying Laplace's equation. A mean value property is derived and experimentally confirmed on phase maps: the mean value on a spherical surface in space is equal to the value at the center of the sphere. Based on this property, a method is implemented for significantly improving the precision of MR phase or field mapping. Three-dimensional mappings of the static magnetic field with a precision of $10^{-11} \sim 10^{-12}$ T are obtained in phantoms by a 1.5-T clinical MR scanner, with about three-orders-of-magnitude precision improvement over the conventional phase mapping technique. *In vivo* **application of the method is also demonstrated on human leg phase maps.**

Key Words: **field mapping; harmonic function; mean value property; phase; SMV.**

In magnetic resonance spectroscopy and imaging, it is desirable to map the magnetic field distribution for shimming procedures (*1, 2*), and the interpretation or correction of artifacts (*3*). Also, a magnetic field map could provide information important for understanding the magnetic susceptibility effects (*3–5*) related to many medical applications such as functional magnetic resonance imaging (*6*), tumor oxygenation measurement (*3, 7*), and bone marrow composition studies (*8*). Magnetic resonance phase imaging (MRPI) is commonly used for mapping the magnetic field (*3, 9, 10*). However, MRPI technology has precision limits of about $10^{-8} \sim 10^{-9}$ T for magnetic field mapping on phantoms and under *in vivo* conditions (*11*).

A harmonic function (*12–14*) u is defined as satisfying Laplace's equation $\nabla^2 u = 0$, commonly used for solving the boundary value problems of static electromagnetic potentials (*15*). In this paper we realize that all of the vector components of the static magnetic fields and the MR phase distribution are harmonic functions in regions with homogeneous magnetic susceptibility (HMS). Based on the mean value property of harmonic functions (*12, 13, 16*), a method is developed for improving the measurement precision for MR phase and static magnetic field signals. By means of gradient echo phase imaging, we generate field maps with high precision up to $10^{-11} \sim 10^{-12}$ T. Such a measurement precision is comparable with that of a superconducting quantum interference device (SQUID) for the magnetic field measurement (*17*). Feasibility with *in vivo* applications is also demonstrated.

THEORY

In free space or regions without susceptibility heterogeneity and no macroscopic currents, all the components of the static magnetic field $\mathbf{H}$ satisfy Laplace's equation, i.e., $\nabla^2 \mathbf{H}_i = 0$, $i = x, y, z$, or $\nabla^2 \mathbf{H} = 0$, which can be easily derived by setting the temporal derivative of the magnetic field in the electromagnetic wave equation (*18*) to zero. Therefore, local magnetic induction (*4, 19*) experienced by a nucleus, $(1 + \chi/3)H$, also satisfies Laplace's equation. Since the spatial distribution of the phase of the MR signal, $\phi(x, y, z)$, linearly corresponds to the z component of magnetic induction assuming no phase aliasing, we have

$$\nabla^2 \phi = 0. \qquad [1]$$

In short, both local magnetic induction and ϕ are harmonic functions in regions with HMS.

The mean value property of harmonic functions (*12, 13, 16*) states that the mean value of a harmonic function u on a spherical space Ω is equal to the value at the center of Ω, i.e.,

$$\text{spherical mean value (SMV)} = u(\mathbf{R}) = \frac{1}{\Lambda} \int_{\Omega} u(\mathbf{R} + \mathbf{r}) d\Omega \qquad [2]$$

in which Ω is either a spherical surface S_r with radius r or a shell V_r with radius r ranging from r_1 to r_2; Λ is either the surface area of S_r or the volume of V_r; $\mathbf{R}$ is at the center of Ω (Fig. 1).

This property directly applies to the local magnetic induction and phase map ϕ in regions with HMS. With Eq. [2] we can effectively reduce the noise in the MR phase and field mea-

1090-7807/01 $35.00

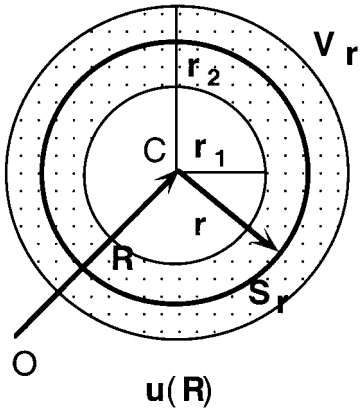

FIG. 1. Harmonic function $u(\mathbf{R})$. S_r is a spherical surface centered at $\mathbf{R}$ $(=\overrightarrow{OC})$ with radius r. V_r is a spherical shell also centered at $\mathbf{R}$ with radius ranging from r_1 to r_2. The function $u(\mathbf{R})$ is equal to the mean value of u on S_r or V_r.

surements. The SMV decreases the random noise of the center value by a factor of the square root of N, the total number of the data points for averaging. For a sphere of radius r in a 3D image data set, $N \approx \frac{4\pi}{3} r^3$. In this paper, the spatial distance is measured by an image unit (i.u.), which is defined as the width of the x dimension of an image pixel or voxel. When r is fixed, the center value, replaced by the average of all the element values in the sphere, has its random noise reduced by a factor of $\sqrt{\frac{4\pi}{3} r^{3/2}}$. With the radius of a typical image size 100 voxels, this is a noise reduction by 2000 times! Thus we can effectively reduce the noise level of the MRPI phase maps with the SMV property to improve the precision for magnetic field measurement.

ANALYSIS AND RESULTS

Three-dimensional phase images of solution phantoms are analyzed with customized Interactive Data Language (IDL) software. Shown in left column of Fig. 2 are typical phase image slices of a typical phantom along three orthogonal directions (transverse, sagittal, and coronal).

Validation of the Harmonic Function Distribution

To verify that the phase distribution is truly a harmonic function in regions of HMS, we employ the Laplace derivative operation (LDO), a convolution of the 3D phase images $u(x, y, z)$ with the Laplacian operator $\hat{\mathbf{L}}$ (*20*), to generate Laplace derivative maps (L-maps). For images with identical spatial resolutions in three orthogonal directions x, y, and z, the discrete form of Laplace's equation is (*21*)

$$\tfrac{1}{6}(u_{1,0,0} + u_{-1,0,0} + u_{0,1,0} + u_{0,-1,0} + u_{0,0,1} + u_{0,0,-1}) - u_{0,0,0} = 0 \qquad [3]$$

in which $u_{i,j,k}$ is the voxel value at the position (i, j, k) $(i, j, k = 0, \pm 1)$, and the center voxel is at the position (0, 0, 0). A $3 \times 3 \times 3$ Laplacian operator is constructed as

$$\hat{\mathbf{L}} = \left\{ \begin{pmatrix} 0 & 0 & 0 \\ 0 & \frac{1}{6} & 0 \\ 0 & 0 & 0 \end{pmatrix}_{k=-1}, \begin{pmatrix} 0 & \frac{1}{6} & 0 \\ \frac{1}{6} & -1 & \frac{1}{6} \\ 0 & \frac{1}{6} & 0 \end{pmatrix}_{k=0}, \begin{pmatrix} 0 & 0 & 0 \\ 0 & \frac{1}{6} & 0 \\ 0 & 0 & 0 \end{pmatrix}_{k=1} \right\}, \qquad [4]$$

and Laplace's equation is equivalent to

$$\hat{\mathbf{L}}u = 0. \qquad [5]$$

Therefore, it is expected that the L-maps have constant zero values throughout the region with HMS and this is demonstrated for phantoms in Fig. 2. Quantitative results from typical 3D regions of interest (ROI) with HMS in phantoms also show

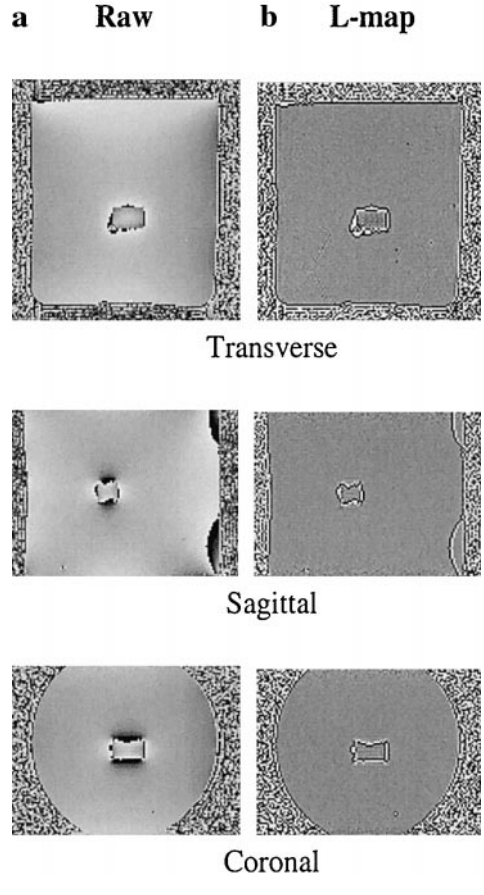

FIG. 2. Comparison of the raw phase maps with the L-maps for the $CuSO_4$ aqueous solution phantom. (a) Typical phase image slices perpendicular to three orthogonal directions (transverse, sagittal, and coronal); all are scaled with identical window size ([0, 2] radians). (b) The L-maps shown with a same window size ([−1, 1] radians). For HMS regions, the L-maps are uniformly zero with standard deviations smaller than that of raw maps.

TABLE 1
Comparison of the Mean and the Standard Deviations (SD) of the Phase Maps and L-Maps from the Typical Phantom Study

ROI[a] and size (voxel)	Raw phase map Mean ± SD (radians)	L-map Mean ± SD (radians)
a: 16 × 16 × 3	1.16 ± 0.047	$-1.4 \times 10^{-4} \pm 0.033$
b: 49 × 32 × 21	1.18 ± 0.27	$4.8 \times 10^{-5} \pm 0.040$
c: 31 × 32 × 7	0.94 ± 0.18	$-2.7 \times 10^{-4} \pm 0.10$
d: 32 × 32 × 32	1.34 ± 0.19	$-2.8 \times 10^{-5} \pm 0.054$

[a] Four typical three-dimensional ROIs with HMS are selected for the calculation.

that the L-maps have mean value very close to zero, two to three orders of magnitude smaller than the standard deviation of the L-maps (Table 1).

We further investigate the mean value property of the phase map with SMV analysis on the 3D phase data. The SMV(r) for a point of interest is calculated by averaging the values of all the image elements on a spherical shell centered at that point. If not stated otherwise, the spherical shells we used for analysis in this work have a thickness of one image unit. The SMV(r) for $r > 1$ i.u. at a center point (x_0, y_0, z_0) is obtained by taking the mean value of those voxels at the coordinates (x, y, z) satisfying $r^2 \leq (x - x_0)^2 + (y - y_0)^2 + (z - z_0)^2 < (r + 1)^2$. For $r = 1$ i.u., from Eq. [5] we have $(\hat{\mathbf{L}} + 1)u = u$. The left-hand side is equivalent to an image convolution by a modified Laplacian derivative operator with zero weight on the central matrix element (0, 0, 0). This means that the value of a central voxel is given by the six neighboring voxels which sit on the three orthogonal directions x, y, and z. Therefore it is justified to define SMV(1) $= (\hat{\mathbf{L}} + 1)u$. For $r = 0$, we define SMV(0) $= u_{0,0,0}$, the value of that voxel itself.

When the center point and the spherical shells with variable radius r are all in the same region of HMS, the SMVs remain constant for all radii (Fig. 3a). The standard deviation of the mean SMV(r), 0.003 rad, is found to be much smaller than the image noise, 0.02 rad.

To examine the aggregate SMV behavior in a typical two-dimensional (2D) ROI (12 by 12 pixels), we calculate mSMV(r), the mean of the SMV values at radius r, for all pixels in that region, the radius r varying from 0 to 15 i.u. When $r = 0$, mSMV(0) is the raw data mean value, equal to 1.471 rad. The fit of mSMV(r) with radius by a constant line (not shown) gives the mean mSMV value 1.468 ± 0.002 rad, in good agreement with mSMV(0) within the noise level of the raw phase map predicted by the mean value property.

High-Precision Field Mapping

Magnetic resonance phase values ϕ can be converted to the z component of local magnetic induction, B_{nmr}, according to $\phi = (\gamma B_{nmr} - \omega_0)$TE, in which ω_0 $(=\gamma B_0)$ is the frequency of the rotating frame and TE is the gradient echo time of MR imaging. Conventionally we adopt the relative field change $\eta = [B_{nmr} - B_0]/B_0$ in units of parts per million (ppm) as the indicator of the field distribution. The relative field η maps for the same 2D ROI in the above section are obtained from the phase values, SMV(r), directly. The field map noise is also calculated, equal to the standard deviation of the difference of an η map and a background polynomial fit (*20*) of the η map. Here the true field distribution is assumed to be varying much more slowly in space than the noise variation. Computer simulations showed that the noise determined from a proper order of polynomial fit is within 10% of the true data noise level (ranging from 0.1 down to 1.0×10^{-6} ppm) for ROIs of sizes at least 10 pixels across.

Generally speaking, the larger the spherical radius r, the greater the number of voxels in the average, and the less the noise of the η map. Actually, the η map noise at radius r, $f(r)$, decreases very quickly from the noise of the raw field map, $f(0) \sim 0.0033$ ppm, to 10 times less as the SMV radius is over three pixels (Table 2). With $N(r)$ as the total number of voxels for SMV at each radius r, we assume

$$f(r) = \frac{a}{\sqrt{N(r)}} + b, \qquad [6]$$

in which a and b are constants and account for raw data noise and systematic errors. The fit of $f(r)$ versus $1/\sqrt{N(r)}$ ($a = 3.25 \times 10^{-3} \pm 9 \times 10^{-5}$ ppm, $b = -7.90 \times 10^{-6} \pm 2 \times 10^{-5}$ ppm) shows a good linear relationship in agreement with Eq. [6] (Fig. 3b).

Figure 4 shows the surface plot of several η maps generated by SMV at increased levels of precision. With the mean value over a whole sphere of a large radius of 20 i.u., the field mapping precision 5×10^{-12} T ($\sim 3.8 \times 10^{-6}$ ppm) is achieved under the 1.5-T main field (Fig. 4f). The method reduces the field mapping noise by three orders of magnitude compared to the raw data without compromising the spatial resolution. For

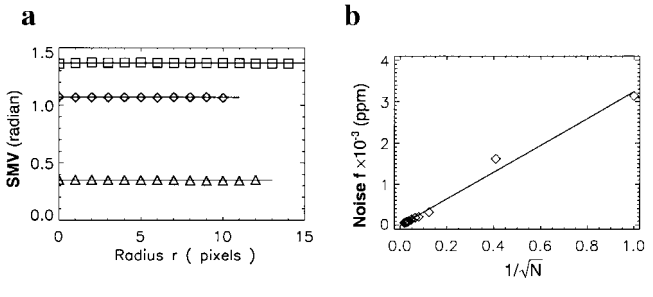

FIG. 3. Spherical mean value analysis. (a) Validation of the SMV property. SMV values are plotted against the radii of the spherical shells for several typical points of interest in the HMS regions under two typical field conditions: (i) the phase map changes monotonously along all x, y, and z axes (△); (ii) the phase map has local field extremities at least along one of the three orthogonal axes (◇ and □). (b) Dependence of the η map noises, f, on the number of pixels in averaging, N. The noise f for a typical 2D ROI (12 × 12 pixels) with HMS is plotted against $1/\sqrt{N}$, with a linear fit correlation coefficient of 0.996.

TABLE 2
The Noise Levels of the Relative Field η Maps Converted from SMV(r) of a Typical 2D ROI in the Phantom

	One-image-unit-thickness spherical shells						Whole sphere	
r (i.u.):	0	1	2	3	6	10	$r = 16$	$r = 20$
N	1	6	66	158	470	1358	17071	33371
$\sqrt{N}$	1	2.45	8.1	12.6	21.7	36.8	131	183
$f(r)$ (ppm)	3.1×10^{-3}	1.6×10^{-3}	3.2×10^{-4}	2.0×10^{-4}	1.2×10^{-4}	8.1×10^{-5}	5.8×10^{-6}	3.8×10^{-6}
$f^*(r)$[a] (ppm)	3.2×10^{-3}	1.3×10^{-3}	3.9×10^{-4}	2.5×10^{-4}	1.4×10^{-4}	8.0×10^{-5}	1.7×10^{-5}	9.9×10^{-6}

[a] $f^*(r)$ is the noise predicted from the linear fit results (Eq. [6]), in good agreement with the real noise $f(r)$. The noise $f(r = 0)$ ($N = 1$) corresponds to SMV(0), the noise of raw maps.

a different field distribution of another ROI, Figs. 4g and 4h show the raw field map and η map at $r = 6$ i.u., respectively. The η map demonstrates substantial precision improvement over the raw field map.

In Vivo Feasibility

We also test the feasibility of applying the SMV method to *in vivo* 3D MR phase maps of human legs. For *in vivo* applications, the HMS condition may not be satisfied, particularly at those transition interfaces between muscle tissues, blood vessels, and bones. However, spaces of scales ranging from several to more than 10 voxels can be found on the L-maps, and they have mean values very close to zero, several orders of magnitude smaller than the L-map standard deviations (Fig. 5). Therefore, the phase distributions in those spaces satisfy Laplace's equation, and the SMV method is used to reduce the noise of the raw magnetic field map by an order of magnitude for a typical 2D ROI shown in Fig. 6.

DISCUSSION AND CONCLUSION

Commonly used data processing methods such as smoothing over a rectangular template or frequency filtering can generate

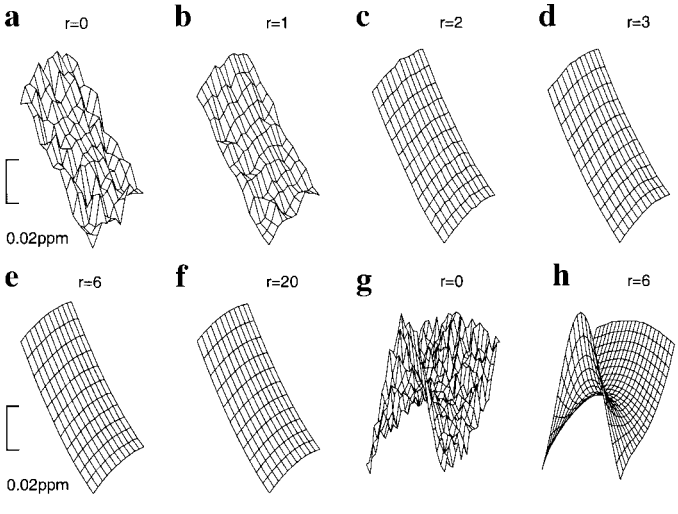

FIG. 4. Improved magnetic field mapping precision for the 2D ROI used in Fig. 3b. (a) The raw field map η from SMV(0) with noise about 0.0033 ppm. (b, c, d, e) High-precision field map obtained from the SMV on the spherical shells with radii spanning from r to $r + 1$, $r = 1, 2, 3, 6$ i.u., respectively. SMV reduces the raw map noise to half at $r = 1$ i.u., 13% at $r = 2$ i.u., less than 10% at $r = 3$ i.u., and 4% at $r = 6$ i.u. (Table 2). (f) The field map obtained by the SMV over the entire sphere of a radius of 20 i.u. The random noise is cut down to 3.8×10^{-6} ppm. (g, h) The raw field map and η map at $r = 6$ i.u. for another ROI with a different field distribution. The two vertical scales on the left indicate 0.02 ppm for the change of the magnetic field.

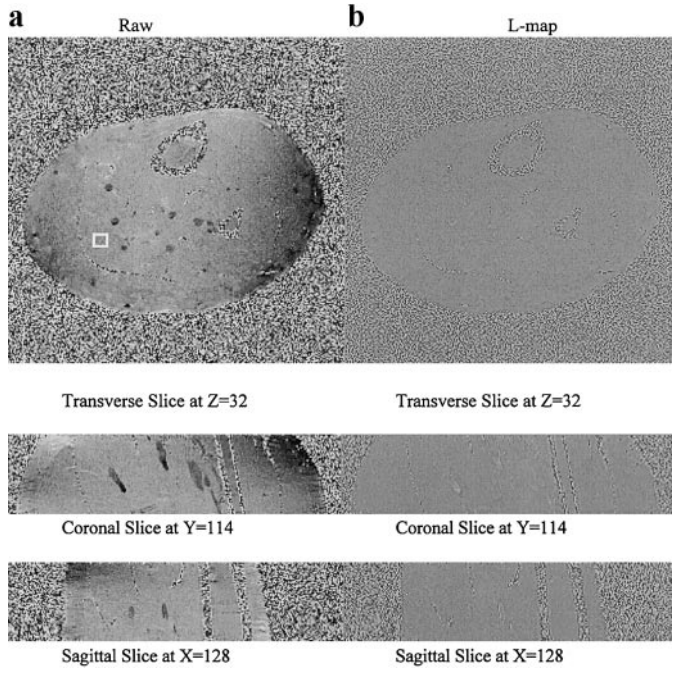

FIG. 5. Application of the Laplace derivative operation to 3D *in vivo* human leg phase images (matrix $256 \times 256 \times 64$). Typical slices of phase maps (column a) and L-maps (column b) along three orthogonal axes (transverse, coronal, and sagittal) are shown with the position indicated by the coordinates. All images are scaled with an identical window size, $[-\pi, \pi]$ radians. Since the raw images have different resolutions along x, y, and z axes ($0.53 \times 0.53 \times 1$ mm, respectively), different scaling factors are introduced for x, y, and z terms in Laplace's equation and the Laplacian operator (see the Appendix). The L-maps are uniformly zero within the noise of raw maps, except at those transition interfaces between muscle tissues, blood vessels, and bones.

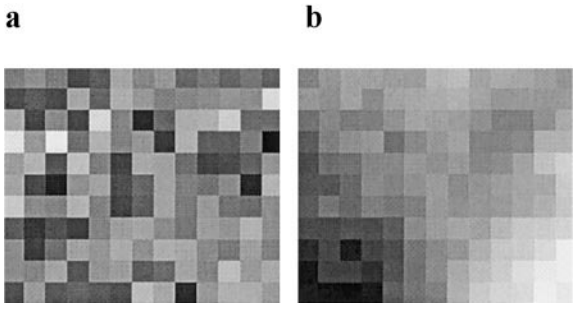

FIG. 6. *In vivo* human leg relative field η maps for a typical 2D ROI (13×11 pixels, corresponding to the white rectangular marker in Fig. 5). (a) The raw field maps. (b) The high-precision field map obtained from SMV analysis on a entire sphere of $r = 4$ i.u. The images are shown with artificially enlarged pixels and a window range of $[-0.05, 0.15]$ ppm. The raw noise is cut down from 0.026 to 0.001 ppm.

images with reduced noise, but these approximation methods may compromise both the spatial resolution and the accuracy because they generally give a biased estimate of the true voxel value. The SMV method is a special smoothing method over spherical regions. Because the mean value property is the intrinsic property of harmonic functions, the SMV method is a smoothing that maintains the correct estimate of the true measurement value for harmonic functions. From first principle and also experimentally confirmed by this work, static magnetic fields and corresponding phase maps are harmonic functions in HMS regions. Applied to these regions, the SMV method produces high-precision field maps. These maps are more accurate than conventional smoothing over a rectangular region (demonstrated by computer simulation).

With the robust spherical mean value method, we cut down the field mapping noise to 5×10^{-12} T (at $r = 20$ i.u.), within the sensitivity range $10^{-10} \sim 10^{-13}$ T of the SQUID (*17*). Compared to SQUID, MRPI has the advantage of 3D field mapping with a spatial resolution of submillimeter. In addition to the application to MR field shimming, the higher precision magnetic field mapping can contribute to the creation of more reliable baselines in phase-encoded MR spectroscopy, and more effective correction of the field inhomogeneity in spectroscopy imaging (*22*). It can also help to correct image distortion artifacts to a more precise extent, and produce higher quality images (*23*).

However, the precision improvements can be compromised near edges where the size of the sphere must be decreased in order to keep the whole sphere in the HMS region. The *in vivo* homogeneity of the magnetic susceptibility can be evaluated with Laplace derivative operation. Our analysis with human leg phase maps suggests that the SMV method is applicable to local *in vivo* regions with a scale as large as 10 voxels. Even with the SMV on a sphere of radius of three voxels, the noise can be reduced to less than 10% of raw data noise (Table 2).

The MR scanner system instability can also limit the precision improvements. When we reduce random noise to a sufficiently small quantity, the system instabilities will manifest themselves, including semirandom or nonrandom factors from both the experimental system and the environment. Presumably these factors are much smaller than the random noise of raw maps. Whereas the SMV method gives us a tool to push the measurement noise down to this lower limit, it also provides us the possibility of examining the system error factors to a better extent by virtually eliminating the random noise.

Phase imaging is sensitive to the field deviations caused by factors such as local eddy currents, temperature fluctuation, and gradient deviations. Their net effects are to overlay shifts on the phase map. Under the experimental condition of this work the phase shift generated by eddy currents is presumably linear with the spatial coordinates (*10*). The Laplacian derivative of a linear function is zero; therefore the phase shift due to eddy currents is a harmonic function. The temperature-induced phase shift is also linear with the temperature change (*11*). The temperature instability comes from environment (<0.1°C) and the milder heating effects of MR sequences. Even when the temperature change is inhomogeneous in the phantom, as long as there are no substantial sources of heat generation or dissipation within the spherical space for SMV analysis, the temperature distribution will obey Laplace's equation $\nabla^2 T = 0$ (*14*). The sources of system imperfection may generate nonlinear gradient deviations, but the sources are not within the homogeneous susceptibility space under study. Therefore, with the presence of eddy currents, temperature fluctuation, and gradient deviations, the phase distribution is still classified as a harmonic function in regions of HMS. This is confirmed by the highly homogeneous L-maps with the mean value deviating from zero only by a small amount on the order of 10^{-4} rad ($\sim 1.6 \times 10^{-5}$ ppm) or less (Table 1), and the constant mean value property shown in the SMV analysis (Fig. 3a). The SMV method can be applied, but the field maps are overlaid with biases due to gradient deviations, eddy currents, and temperature fluctuations. The biases can presumably be canceled out with controls when only relative field or phase changes are of interest for most applications. Actually the methods in this paper make it feasible for a more precise quantitation of the effects on field maps by these factors. For example, take the difference of the high-precision maps before and after turning on a magnetic gradient, and the quantitative effect of eddy currents from this gradient can be obtained with improved accuracy.

In addition to the precision improvement and the evaluation of systematic factors, the method can be used for the artifact correction on phase maps as well. Due to factors such as motion and flow, there are localized artifacts and smears on the phase maps. Generally speaking, for unknown data at a point of interest on phase images, we can actually obtain the true value of this point by taking the average of all the image element values on a spherical surface or shell surrounding it, when the assumption of the harmonic function is valid throughout that whole spherical region.

We have demonstrated theoretically and experimentally that magnetic field components and the phase distribution in a uniform magnetic susceptibility region are harmonic functions. We further developed the general methodology of precision improvement based on the mean value property of harmonic functions. The precision of the 3D MR phase and magnetic field mapping can be substantially improved both in phantoms and *in vivo.*

EXPERIMENTAL

Experimental phantoms consist of one or more small boxes (various shapes such as cylindrical and rectangular, and sizes of a few centimeters, filled with 0.03 $\sim$ 0.1 M aqueous $CuSO_4$ solution) glued to a thin plastic supporting frame mounted in a large beaker. The beaker is filled with much less concentrated copper sulfate aqueous solution ($<10^{-2}$ M). The susceptibility difference between the inside and outside the small box contributes to the magnetic field inhomogeneity in the phantom.

Three-dimensional fast-low-angle-shot (FLASH) images of the phantoms were obtained with a head coil on a Siemens 1.5-T clinical MR scanner ($\gamma B_0/2\pi = 63.59$ MHz). The imaging parameters for the phantoms are TR/TE 40/15 ms, flip angle 30°, matrix 128 × 128 × 128, resolution 1 × 1 × 1 mm, and single excitation. The *in vivo* 3D phase maps were acquired for a thick transverse section of the small leg of a female human subject, with imaging parameters TR/TE 40/15 ms, flip angle 30°, matrix 256 × 256 × 64, resolution 0.53 × 0.53 × 1 mm, and single excitation. The original FLASH phase images appear with zebra stripes because of the asymmetrical gradient echoes. They are restored to normal images with customized IDL software by shifting the central positions of the MR gradient echo signals in the *k* space before the Fourier transform. Then the phase maps were used for data analysis.

APPENDIX

Construction of the 3D Laplace Derivative Operator $\hat{\mathbf{L}}$

From Laplace's equation

$$\frac{\partial^2 u}{\partial x^2} + \frac{\partial^2 u}{\partial y^2} + \frac{\partial^2 u}{\partial z^2} = 0, \qquad [1]$$

we consider the discreet form of the equation at the position (0,0,0) ($u_{i,j,k}$ is the value of the voxel at the position (i, j, k) (i, j, $k = 0, \pm 1$)),

$$\frac{\partial^2 u}{\partial x^2} = \frac{\dfrac{u_{1,0,0} - u_{0,0,0}}{\Delta x} - \dfrac{u_{0,0,0} - u_{-1,0,0}}{\Delta x}}{\Delta x} = \frac{u_{1,0,0} + u_{-1,0,0} - 2u_{0,0,0}}{(\Delta x)^2}. \qquad [2]$$

Similarly

$$\frac{\partial^2 u}{\partial y^2} = \frac{u_{0,1,0} + u_{0,-1,0} - 2u_{0,0,0}}{(\Delta y)^2}$$

$$\frac{\partial^2 u}{\partial z^2} = \frac{u_{0,1,0} + u_{0,-1,0} - 2u_{0,0,0}}{(\Delta z)^2}. \qquad [3]$$

Assume that $\Delta x = \delta$, $\frac{\Delta x}{\Delta y} = \lambda_1$, and $\frac{\Delta x}{\Delta z} = \lambda_2$; then

$$\begin{aligned}\nabla^2 u &= \frac{u_{1,0,0} + u_{-1,0,0} - 2u_{0,0,0}}{\delta^2} + \lambda_1^2 \cdot \frac{u_{0,1,0} + u_{0,-1,0} - 2u_{0,0,0}}{\delta^2} + \lambda_2^2 \cdot \frac{u_{0,0,1} + u_{0,0,-1} - 2u_{0,0,0}}{\delta^2} \\ &= \frac{1}{\delta^2}[(u_{1,0,0} + u_{-1,0,0}) + \lambda_1^2(u_{0,1,0} + u_{0,-1,0}) + \lambda_2^2(u_{0,0,1} + u_{0,0,-1}) - 2(1 + \lambda_1^2 + \lambda_2^2)u_{0,0,0}] \\ &= 0 \end{aligned} \qquad [4]$$

$$u_{1,0,0} + u_{-1,0,0} + \lambda_1^2(u_{0,1,0} + u_{0,-1,0}) + \lambda_2^2(u_{0,0,1} + u_{0,0,-1}) - 2(1 + \lambda_1^2 + \lambda_2^2)u_{0,0,0} = 0. \qquad [5]$$

Normalize the coefficient of $u(0, 0, 0)$ to one, and we have

$$\frac{1}{2(1 + \lambda_1^2 + \lambda_2^2)}(u_{1,0,0} + u_{-1,0,0}) + \frac{\lambda_1^2}{2(1 + \lambda_1^2 + \lambda_2^2)}(u_{0,1,0} + u_{0,-1,0}) + \frac{\lambda_2^2}{2(1 + \lambda_1^2 + \lambda_2^2)}(u_{0,0,1} + u_{0,0,-1}) - u_{0,0,0} = 0. \qquad [6]$$

The Laplacian operator $\hat{\mathbf{L}}$ is a 3 × 3 × 3 matrix; the components are

$$\hat{L}_{3,z=\pm 1} = \begin{pmatrix} 0 & 0 & 0 \\ 0 & 0.5\lambda_2^2/(1 + \lambda_1^2 + \lambda_2^2) & 0 \\ 0 & 0 & 0 \end{pmatrix}$$

$$\hat{L}_{3,z=0} = \begin{pmatrix} 0 & 0.5\lambda_1^2/(1 + \lambda_1^2 + \lambda_2^2) & 0 \\ 0.5/(1 + \lambda_1^2 + \lambda_2^2) & -1 & 0.5/(1 + \lambda_1^2 + \lambda_2^2) \\ 0 & 0.5\lambda_1^2/(1 + \lambda_1^2 + \lambda_2^2) & 0 \end{pmatrix}. \qquad [7]$$

If $\lambda_1 = \lambda_2 = 1$ in Eq. [6]

$$\tfrac{1}{6}(u_{1,0,0} + u_{-1,0,0} + u_{0,1,0} + u_{0,-1,0} + u_{0,0,1} + u_{0,0,-1}) - u_{0,0,0} = 0 \qquad [8]$$

then

$$\hat{\mathbf{L}} = \left\{ \begin{pmatrix} 0 & 0 & 0 \\ 0 & \frac{1}{6} & 0 \\ 0 & 0 & 0 \end{pmatrix}_{z=-1}, \begin{pmatrix} 0 & \frac{1}{6} & 0 \\ \frac{1}{6} & -1 & \frac{1}{6} \\ 0 & \frac{1}{6} & 0 \end{pmatrix}_{z=0}, \begin{pmatrix} 0 & 0 & 0 \\ 0 & \frac{1}{6} & 0 \\ 0 & 0 & 0 \end{pmatrix}_{z=1} \right\}. \qquad [9]$$

For image analysis, Laplace's equation is equivalent to a convolution of $\hat{\mathbf{L}}$ with u

$$\hat{\mathbf{L}} \otimes u = 0 \quad \text{or} \quad \hat{\mathbf{L}}u = 0. \qquad [10]$$

We define the Laplace derivative operation (LDO) as $\hat{\mathbf{L}} \otimes u$ or $\hat{\mathbf{L}}u$, which produces the homogeneous Laplace derivative map (L-map) with expected zero value.

ACKNOWLEDGMENTS

We are very thankful to Dr. Z. J. Wang and Dr. John Haselgrove of the Children's Hospital of Philadelphia for their suggestions and assistance. This work is supported by a grant from NIH (RR02305) in the United States.

REFERENCES

1. M. G. Prammer, J. C. Haselgrove, M. Shinnar, and J. S. Leigh, *J. Magn. Reson.* **77,** 40–52 (1988).
2. I. S. Mackenzie, E. M. Robinson, A. N. Wells, and B. Wood, *Magn. Reson. Med.* **5,** 262–268 (1987).
3. D. D. Stark and W. G. Bradley, Jr., "Magnetic Resonance Imaging," Mosby–Year Book, Boston (1992).
4. S. C. Chu, Y. Xu, J. A. Balschi, and C. S. Springer, Jr., *Magn. Reson. Med.* **13,** 239–262 (1990).
5. O. Beuf, A. Briguet, M. Lissac, and R. Davis, *J. Magn. Reson. B* **112,** 111–118 (1996).
6. P. C. M. van Zijl, S. M. Eleff, J. A. Ulatowski, J. M. E. Oja, A. M. Ulug, R. J. Traystman, and R. A. Kaupoinen, *Nature* **4,** 159–167 (1998).
7. R. Mazurchuk, R. Zhou, R. Straubinger, R. Chau, and Z. Grossman, *Magn. Reson. Imaging* **17,** 537–548 (1999).
8. F. Schick, *J. Magn. Reson. B* **108,** 1–11 (1995).
9. I. J. Cox, b.G.M., D. G. Gadian, I. R. Young, E. Proctor, S. R. Williams, and I. Hart, *J. Magn. Reson.* **70,** 163–168 (1986).
10. Y. S. Kim and Z. H. Cho, *J. Magn. Reson.* **78,** 459–471 (1988).
11. Y. Ishihara, A. Calderon, H. Watanabe, K. Okamoto, Y. Suzuki, K. Kuroda, and Y. Suzuki, *Magn. Reson. Med.* **34,** 814–823 (1995).
12. S. Axler, P. Bourdon, and W. Ramey, "Harmonic Function Theory," Springer-Verlag, New York (1992).
13. S. Lang, "Complex Analysis," pp. 224–243, Springer-Verlag, New York (1985).
14. R. V. Churchill and J. W. Brown, "Complex Variables and Applications," pp. 233–241, McGraw–Hill, New York (1984).
15. J. D. Jackson, "Classical Electrodynamics," Wiley, New York (1998).
16. E. M. Purcell, "Electricity and Magnetism," p. 61, McGraw–Hill, New York (1963).
17. D. Craik, "Magnetism: Principles and Applications," pp. 418–420, Wiley, New York (1995).
18. R. P. Feynman, R. B. Leighton, and M. Sands, "The Feynman Lectures on Physics," Addison–Wesley, New York (1964).
19. Z. J. Wang, S. Li, and J. C. Haselgrove, *J. Magn. Reson.* **140,** 477–481 (1999).
20. J. C. Russ, "The Image Processing Handbook," pp. 184–227, CRC Press, Boca Raton, FL (1994).
21. A. A. Kaufman, "Geophysical Field Theory and Method, Part A," pp. 88–91, Academic Press, San Diego (1992).
22. A. A. Maudsley and S. K. Hilal, *Magn. Reson. Med.* **2,** 218–233 (1985).
23. J. Weis, A. Ericsson, and A. Hemmingsson, *Magn. Reson. Imaging* **16,** 839–844 (1998).